Supporting information

Dynamic Cu Valence State Cycling Regulates Urea-OH^- Adsorption Competition: Electrocatalytic Mechanism and Application of Cu_xS/FeS/NF

Wensong Wang,[a] Ying Tian,[a] Xiuwen Cao,[a] Xiang Liu,[a] Shizhe Cao,[a] Deheng Chen,[a] Weizi Jiang,[a] Mingtao Li,[a] Weiwei Lin,[d] Xun Sun*,[e] Shenjie Li*[a][b][c], and Yanyan Chen*[a][b][c]

[a] *School of Chemistry and Chemical Engineering, Hefei University of Technology, Hefei, 230009, PR China*

[b] *Anhui Province Key Laboratory of Value-Added Catalytic Conversion and Reaction Engineering, Hefei University of Technology, Hefei, 230009, PR China*

[c] *Anhui Province Engineering Research Center of Flexible and Intelligent Material, Hefei University of Technology, Hefei, 230009, PR China*

[d] *Anhui Laboratory of Clean Catalytic Engineering, Anhui Polytechnic University, Wuhu, 241000, PR China*

[e] *School of Carbon Neutrality Science and Engineering, Aust Hefei Institute for Advanced Research, Anhui University of Science and Technology, Hefei, 231131, PR China*

Contents

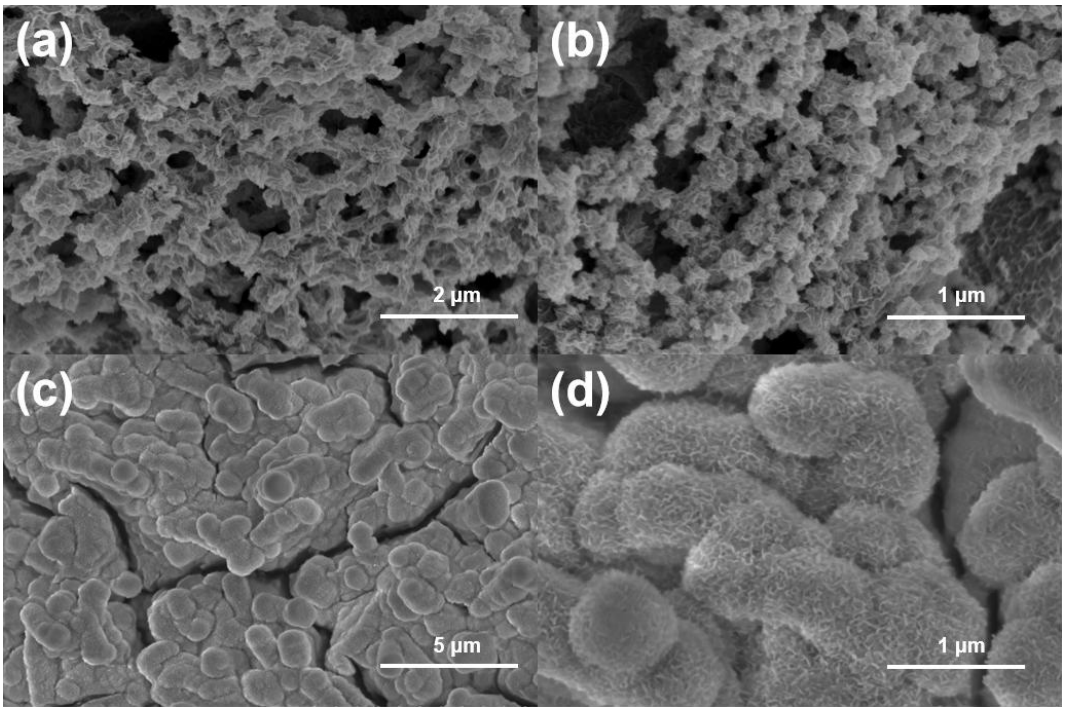

Figure S1. SEM images of Fe-MOF/NF (a, b) and 20-Cu_xS/FeS/NF (c, d).

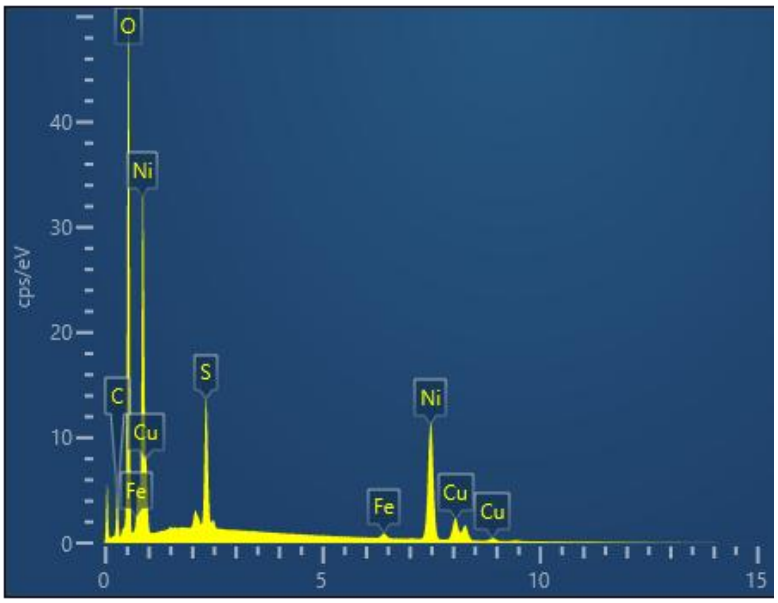

Figure S2. Elemental mapping images of 20-Cu_xS/FeS/NF.

Table S1. EDS-Determined Elemental Composition of the 20-Cu_xS/FeS/NF Composite.

Element	Sample 20-Cu_xS/FeS/NF	
	Wt%	At%
Ni	40.67	16.88
O	32.90	50.10
C	12.80	25.99
Cu	8.07	3.09
S	4.71	3.58
Fe	0.84	0.35
Total	100.00	

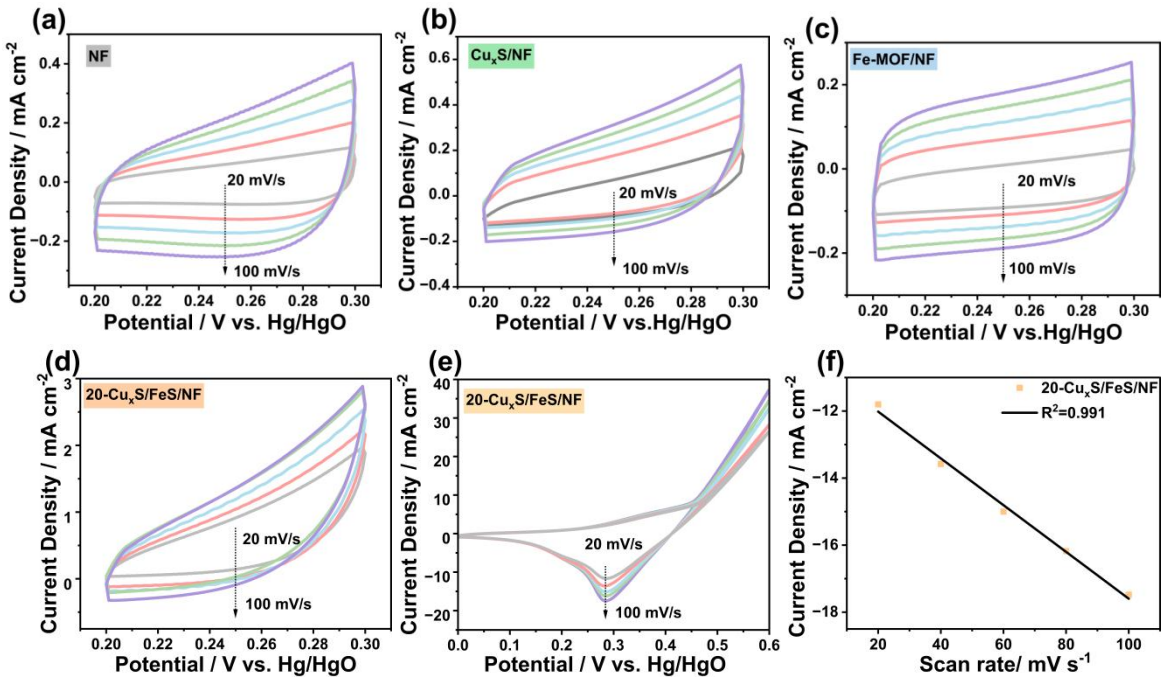

Figure S3. Subplots of cyclic voltammetry (CV) curves for different samples in a mixed electrolyte of 1 M KOH and 0.33 M urea. (a), (b), (c), and (d) correspond to the CV curves of nickel foam (NF), Cu_xS/NF, Fe-MOF/NF, and 20-Cu_xS/FeS/NF within the non-Faradaic region, respectively, with a test scan rate range of 20-100 mV/s and a reference electrode of Hg/HgO. Subplot (e) shows the CV curves of 20-Cu_xS/FeS/NF within the Faradaic region, with the same test scan rate and potential reference conditions as above. (f) Further analysis of the relationship between the peak current of the active Cu species reduction peak and the scan rate in this subplot reveals a strict linear correlation (correlation coefficient $R^2 = 0.991$).

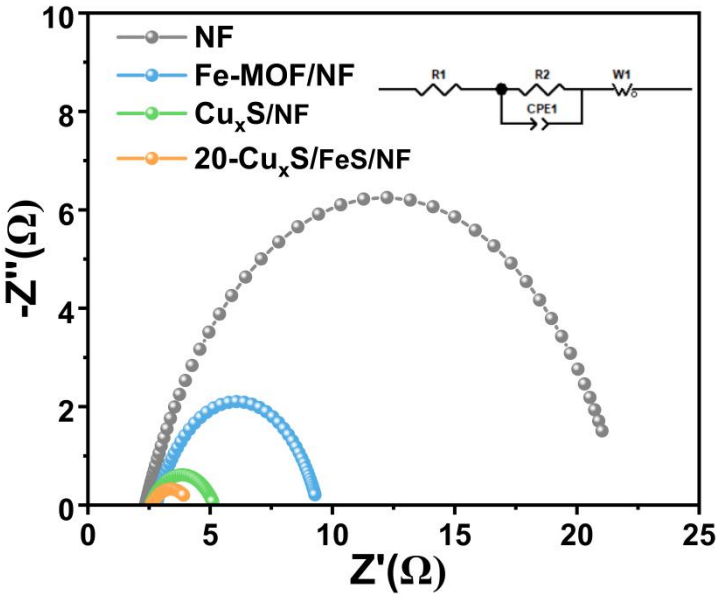

Figure S4. Nyquist plots of NF, Fe-MOF/NF, Cu_xS/NF and 20-Cu_xS/FeS/NF at the same potential (1.43 V vs. RHE).

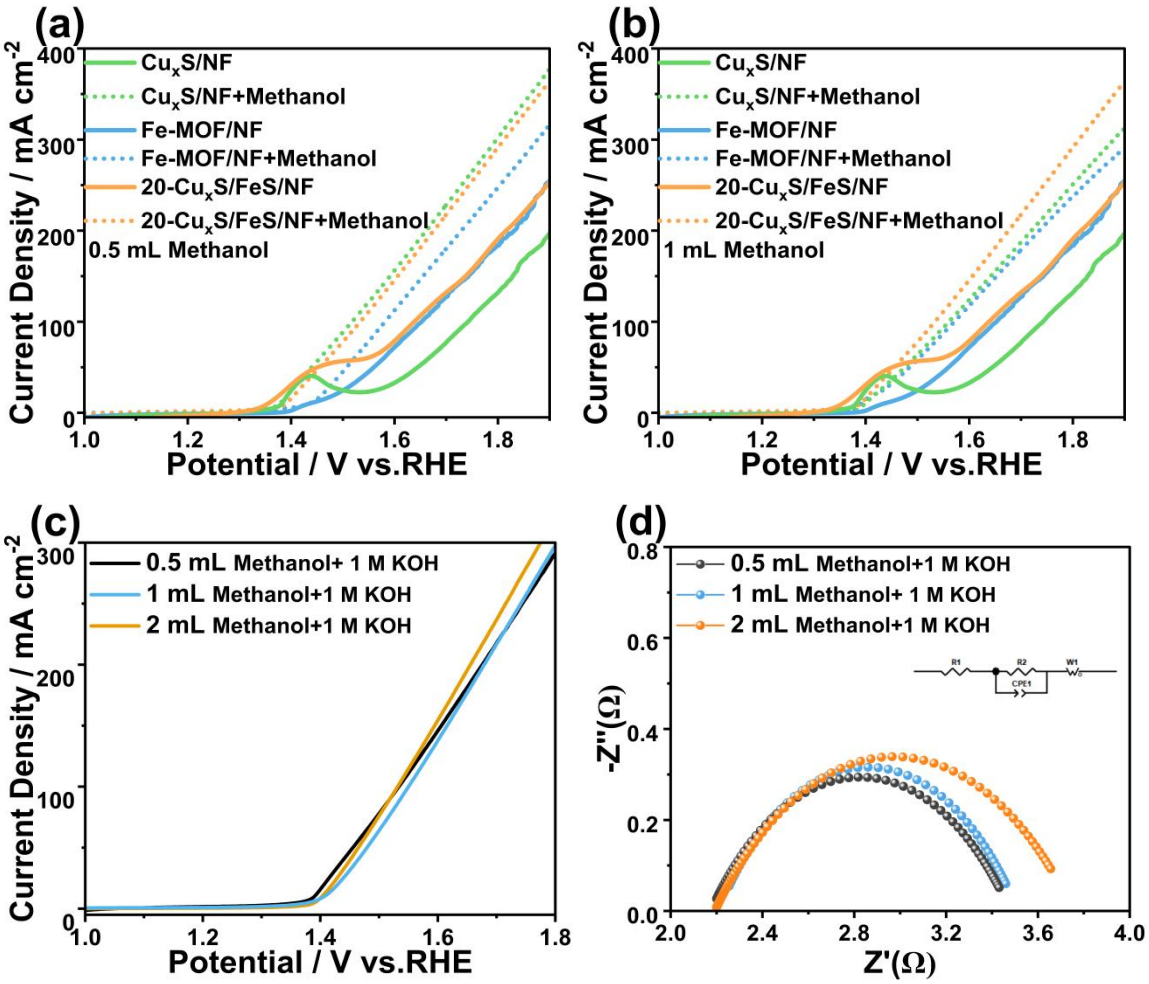

Figure S5. Polarization curves in 1 M KOH with/without methanol of Fe-MOF/NF, Cu_xS/NF, and 20-Cu_xS/FeS/NF: (a) 0.5 mL methanol; (b) 1 mL methanol. (c) Polarization curves and (d) Electrochemical impedance spectra (EIS) of 20-Cu_xS/FeS/NF in 1 M KOH solution with the addition of 0.5 mL, 1 mL, and 2 mL of methanol, respectively.

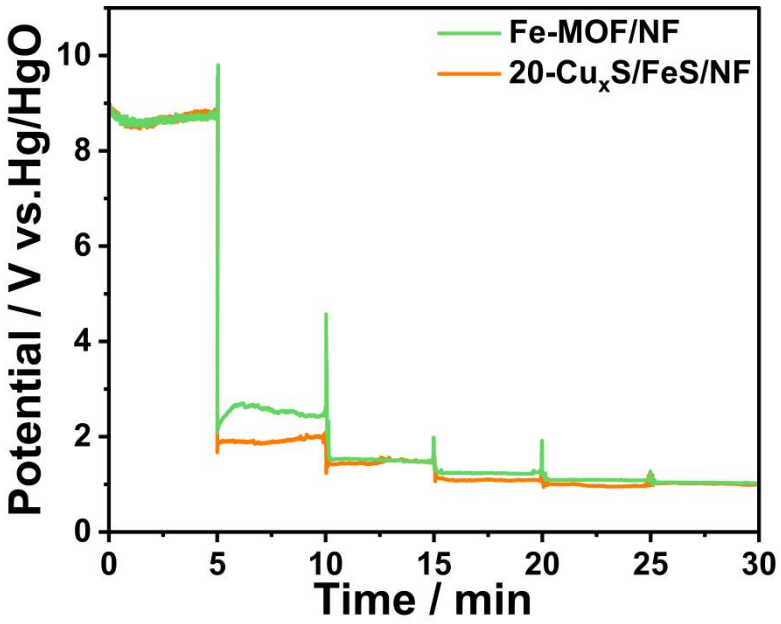

Figure S6. The galvanostatic potential curves of 20-Cu_xS/FeS/NF and Fe-MOF/NF were measured in a basic electrolyte containing urea, using a constant current mode. KOH was gradually added to the system during the test to dynamically regulate its concentration, while simultaneously recording and displaying the potential-time response behaviors of both samples under these dynamic conditions.

Table S2. The Concentration of KOH, and pH value of the solution after sequential addition of KOH in the original experiment and the corresponding current density of two catalysts reported in Figure 3h.

Times	Concentration of KOH (mol/L)	pH value of electrolyte	Current density (mA cm^{-2})	
			Fe-MOF/NF	20-Cu_xS/FeS/NF
0	0.000	6.53	0.05	0.05
1	0.039	12.6	4.7	7.8
2	0.078	12.9	9.5	10.9
3	0.117	13.06	14.5	15.8
4	0.154	13.16	19.2	21.1
5	0.190	13.25	24.0	25.9
6	0.226	13.32	28.5	30.1
7	0.262	13.38	33.7	34.5
8	0.296	13.43	38.3	38.9
9	0.330	13.47	43.9	43.1

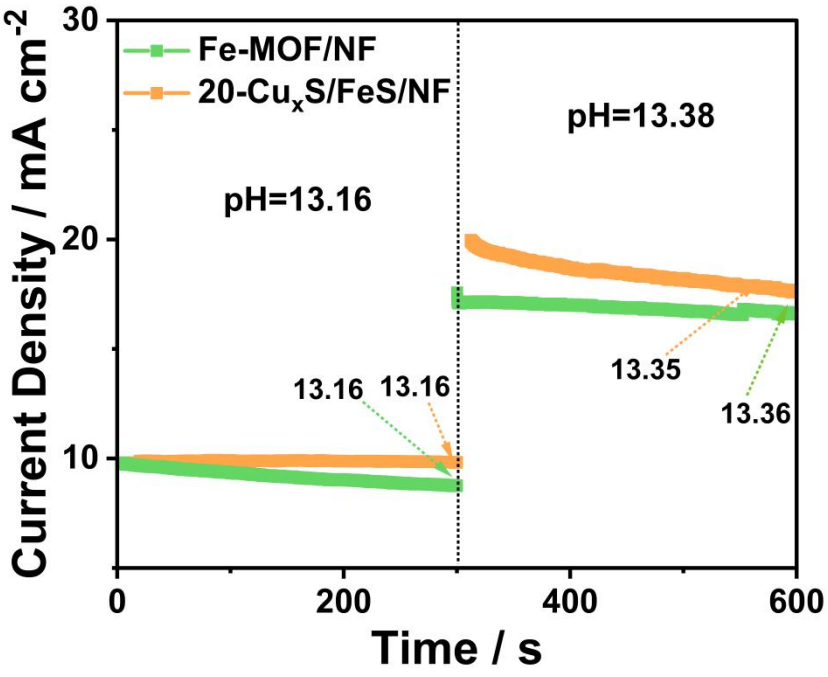

Figure S7. I-t plots under the conditions of the 4th addition (pH = 13.16) and the 7th addition (pH = 13.38).

Table S3. Comparison of chronoamperometric performance between two catalysts under fixed pH conditions.

catalyst	pH values of			The extent of the decrease in pH value
	electrolyte	Before UOR	After UOR	
20-Cu_xS/FeS/NF	13.16	13.16	13.16	0
Fe-MOF/NF	13.16	13.16	13.16	0
20-Cu_xS/FeS/NF	13.38	13.38	13.35	0.0022
Fe-MOF/NF	13.38	13.38	13.36	0.0015

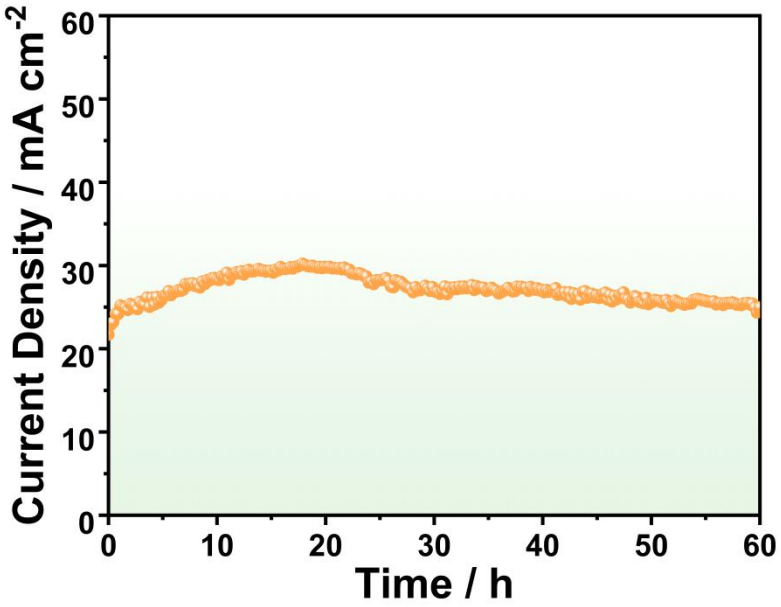

Figure S8. Chronoamperometric (i-t) curve of 20-Cu_xS/FeS/NF.

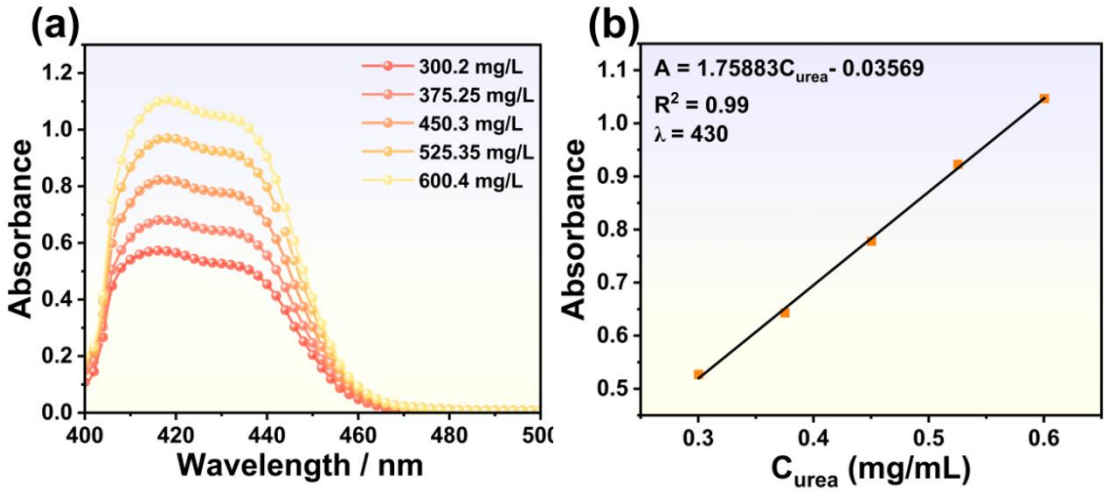

Figure S9. (a) UV-vis absorption spectra of urea solutions with different concentration. (b) The corresponding UV-vis standard calibration curve for urea concentration.

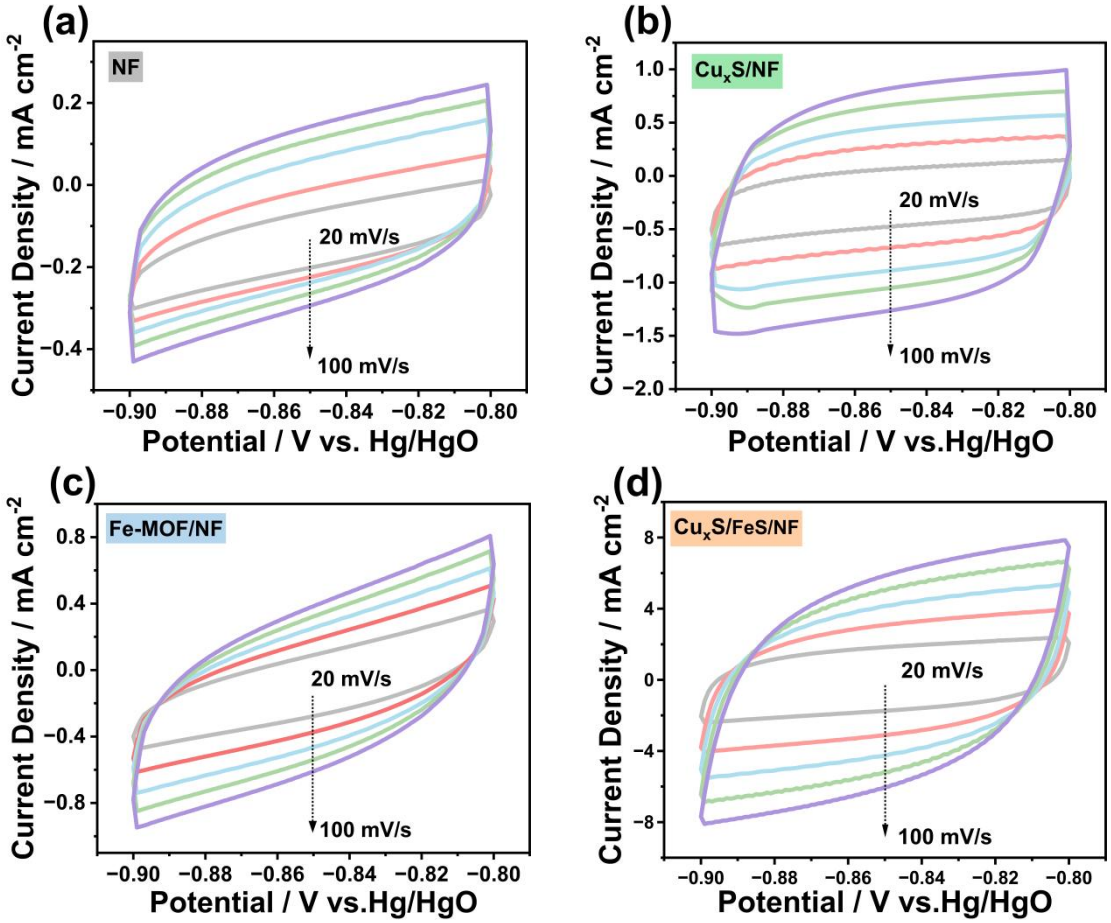

Figure S10. CV curves of NF(a), Cu_xS/NF (b), Fe-MOF/NF(c) and 20-Cu_xS/FeS/NF (d) at scan rates from 20 to 100 mV/s, with potential versus Hg/HgO in 1 M KOH.

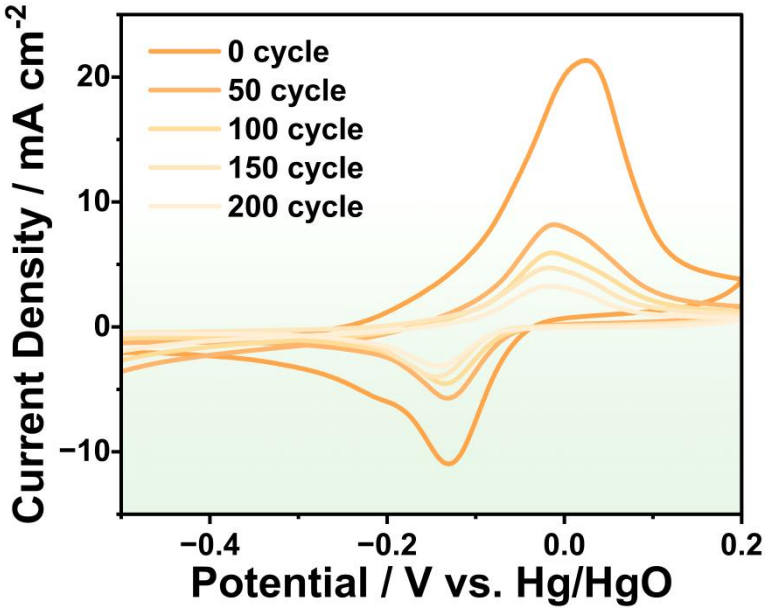

Figure S11. CV cycles of Cu_xS/FeS/NF after different activation cycles in 1 M KOH and 0.33 M urea.

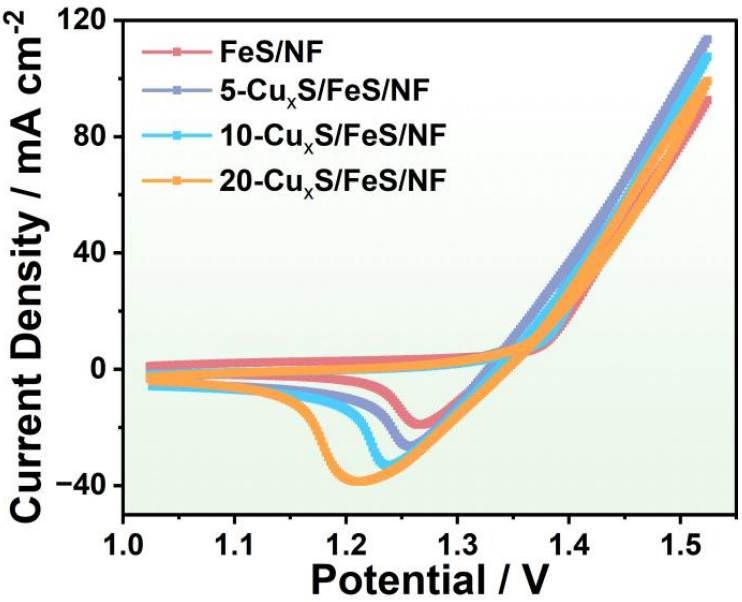

Figure S12. CV curves of FeS/NF, 5-Cu_xS/FeS/NF, 10-Cu_xS/FeS/NF and 20-Cu_xS/FeS/NF in 1 M KOH and 0.33 M urea at 0 V -0.6 V (vs. RHE).

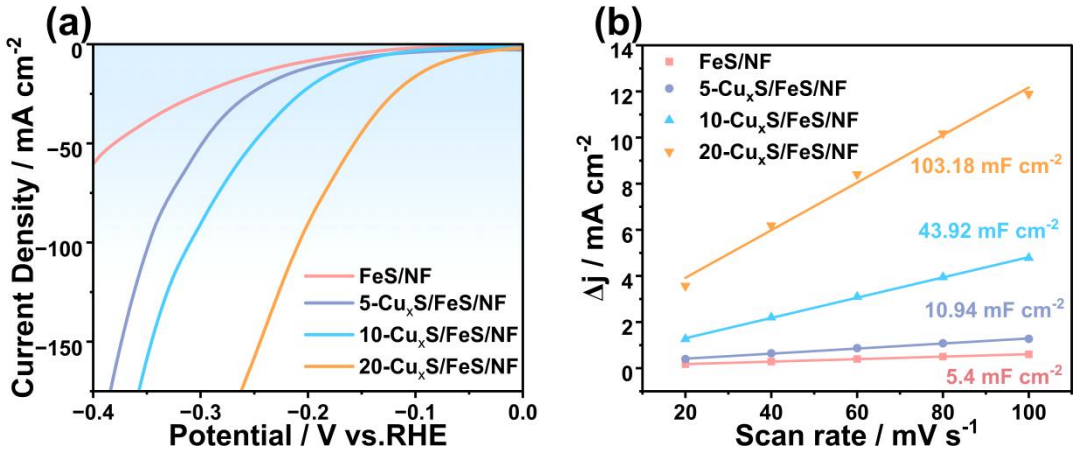

Figure S13. (a) LSV curves and (b) C_{dl} values of FeS/NF, 5-Cu_xS/FeS/NF, 10-Cu_xS/FeS/NF, and 20-Cu_xS/FeS/NF for HER.

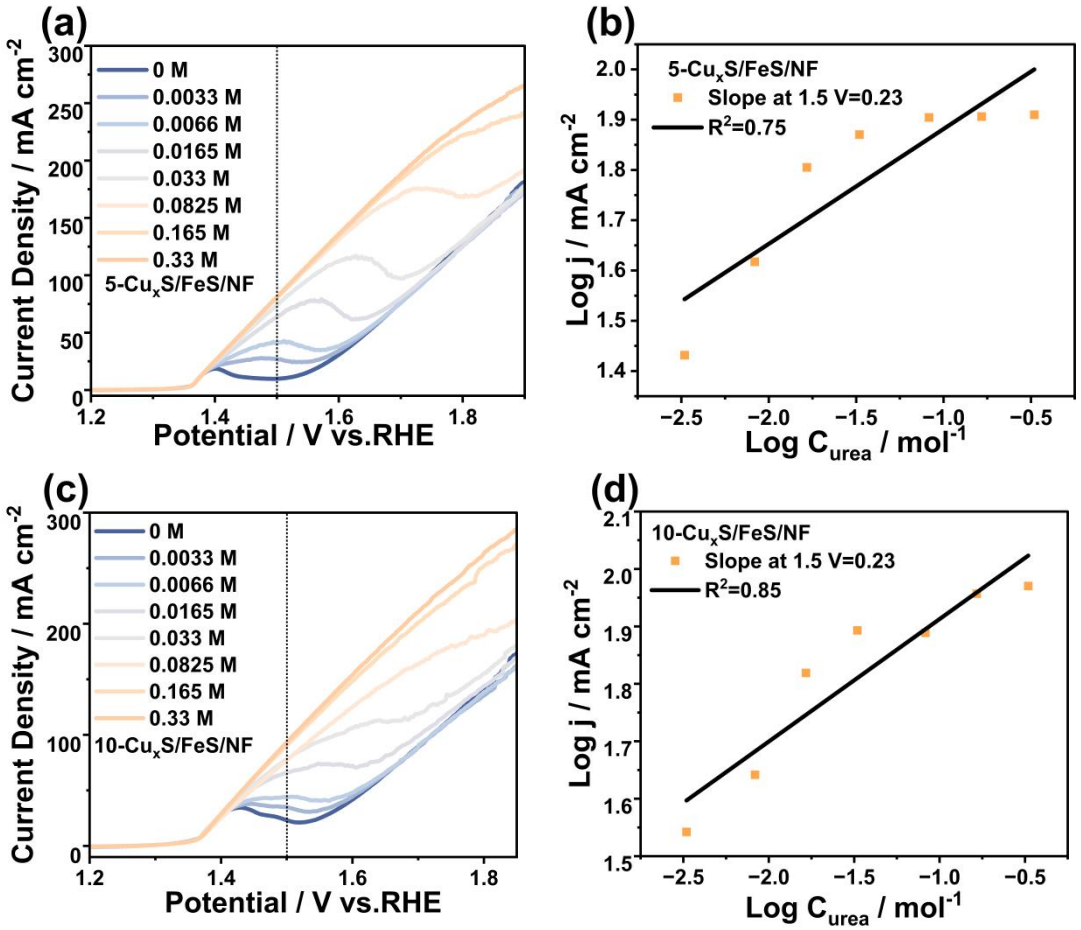

Figure S14. LSV curves of 5-Cu_xS/FeS/NF (a) and 10-Cu_xS/FeS/NF (c) in 1 M KOH with different urea concentrations (0 M, 0.0033 M, 0.0066 M, 0.0165 M, 0.033 M, 0.0825 M, 0.165 M, 0.33 M) and the corresponding kinetic indices (b and d) at 1.5 V (vs. RHE).

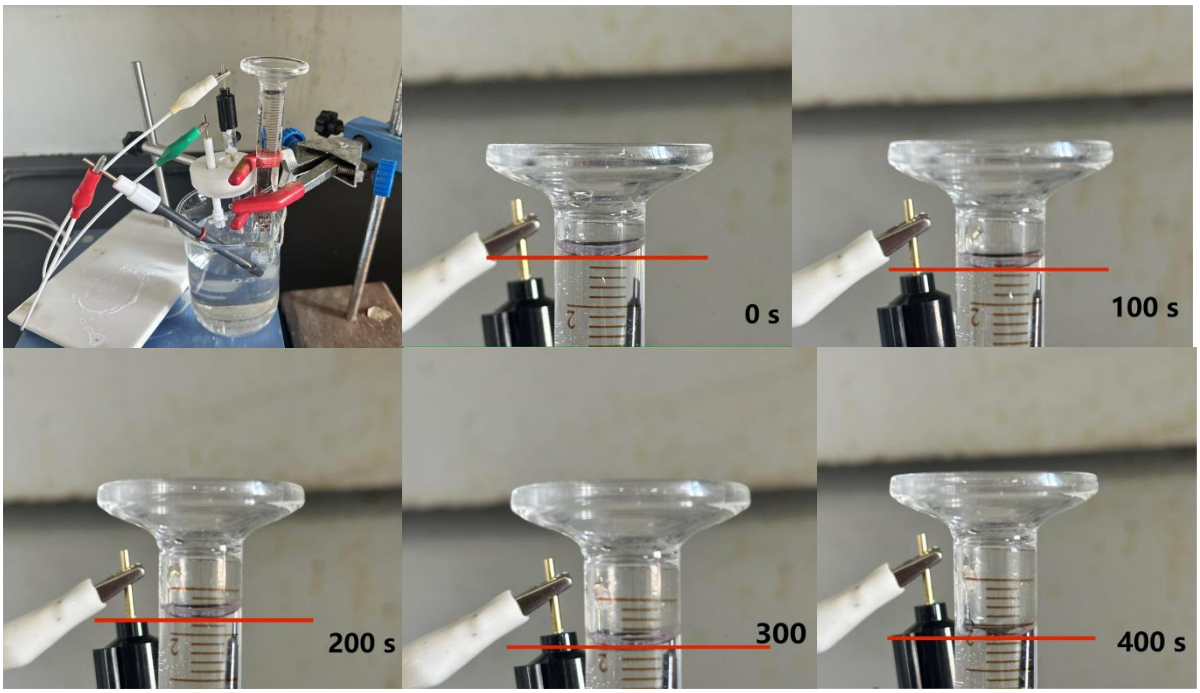

Figure S15. Faraday efficiency Measurement Setup of 20-Cu_xS/FeS/NF and hydrogen collection by drainage method diagram.

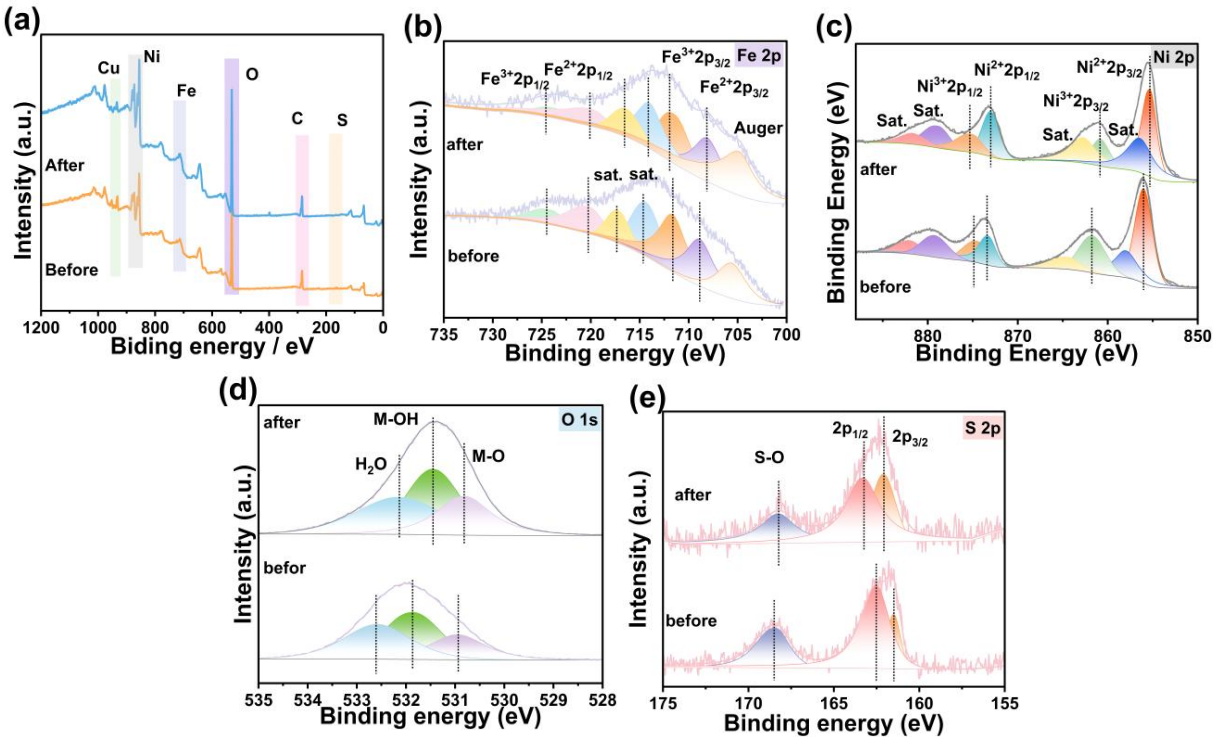

Figure S16. XPS spectra of 20-Cu_xS/FeS/NF after 60-hour stability test in UOR: (a) survey scan, (b) Fe 2p, (c) Ni 2p, (d) O 1s, and (e) S 2p.

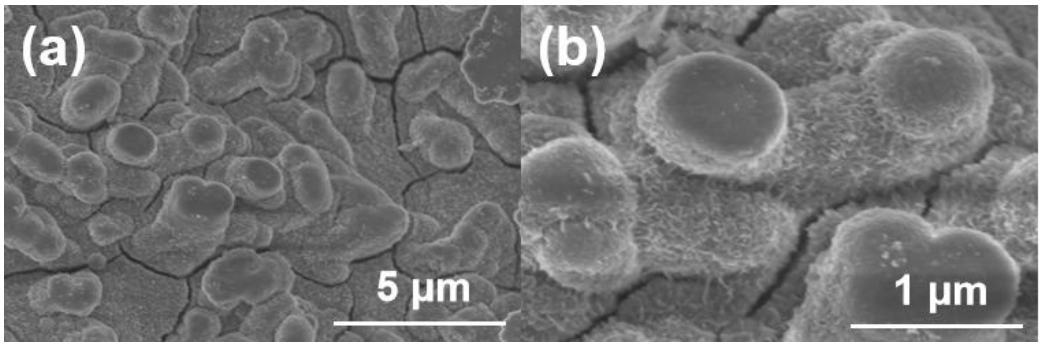

Figure S17. SEM images of 20-Cu_xS/FeS/NF after 60-hour UOR stability test under 5 μm (a) and 1 μm (b) scale.

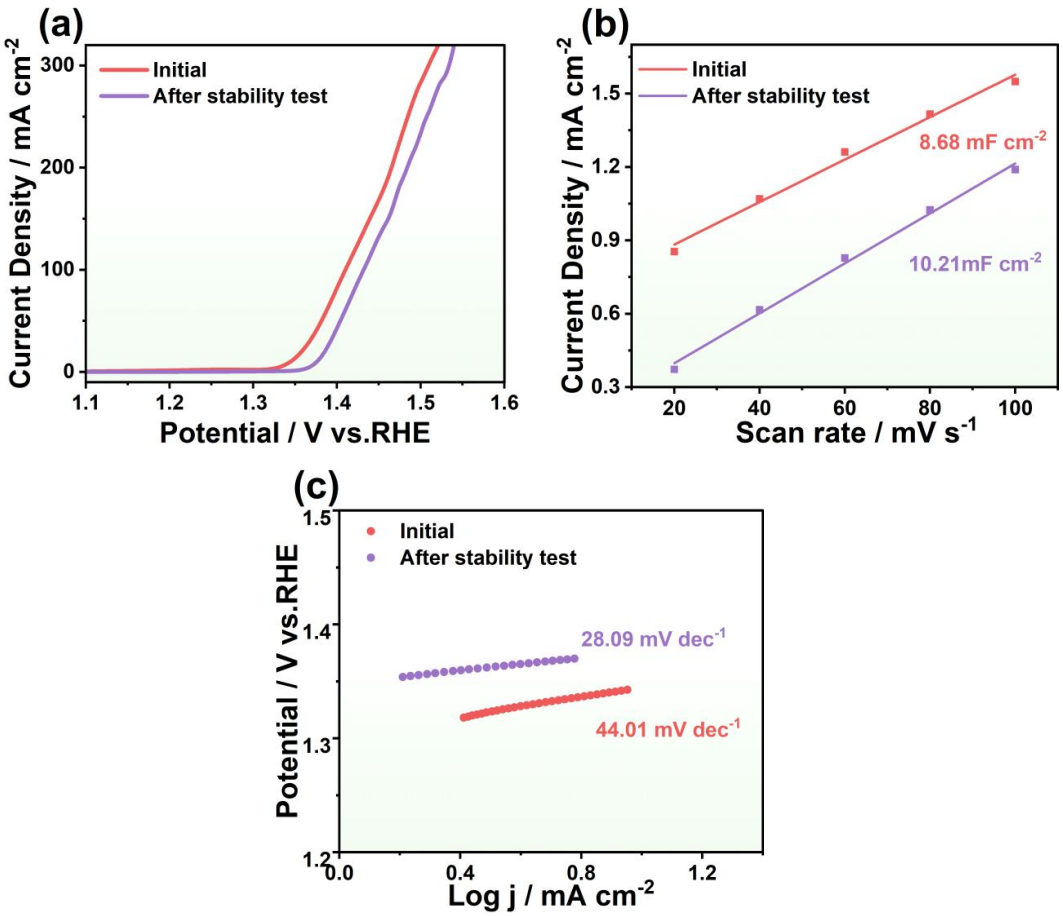

Figure S18. The electrochemical performence of 20-Cu_xS/FeS/NF before and after 60-h-UOR testing: (a) LSV curves, (b) double-layer capacitance (Cdl), and (c) Tafel plots.

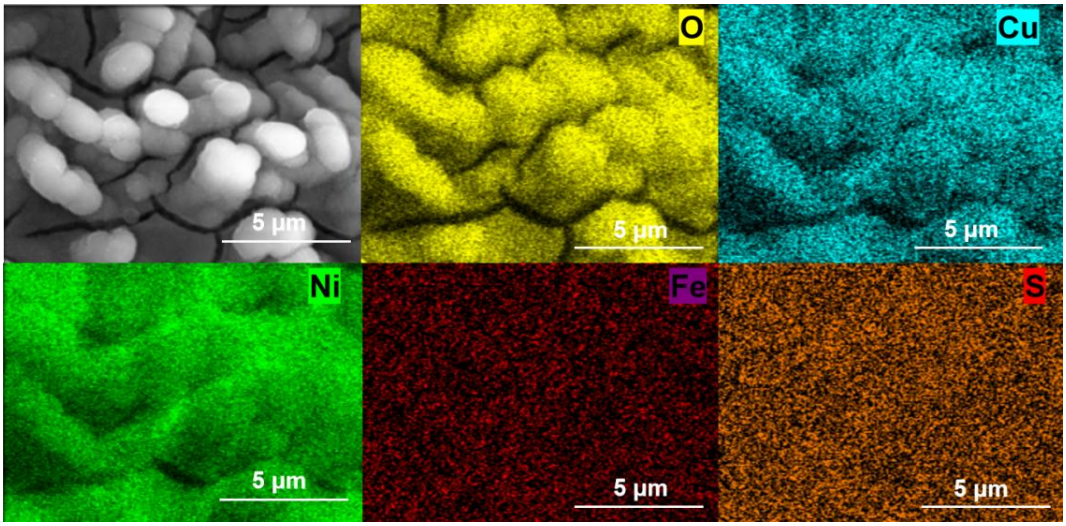

Figure S19. Elemental mapping of 20-Cu_xS/FeS/NF after 60 h UOR stability test.

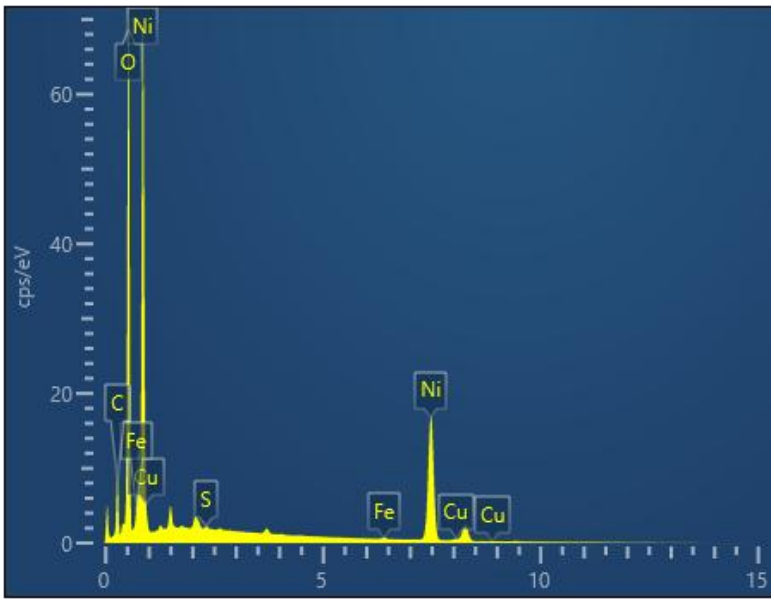

Figure S20. Elemental mapping of 20-Cu_xS/FeS/NF after stability testing.

Table S4. EDS-Determined Elemental Composition of the 20-Cu_xS/FeS/NF after stability testing.

Element	Sample Cu_xS/FeS/NF	
	Wt%	At%
Ni	59.82	26.617
O	27.59	45.031
C	12.80	27.856
Cu	0.61	0.251
S	0.11	0.121
Fe	0.33	0.154
Total	100.00	

Table S5. Recently Reported Catalysts for Electrochemical Urea Oxidation Reaction (UOR//HER) Performance Evaluation.

Samples	Performance	References
NiSe-Ni_3S_2/GNF	1.54 V vs. RHE@50 mA cm^{-2}	[1]
Ni_{100}-W_1-NF	1.56 V vs. RHE@100 mA cm^{-2}	[2]
Sv-CoNiS@NF	1.65 V vs. RHE@50 mA cm^{-2}	[3]
NiCoV-LDH/rGO/NF-100	1.45 V.vs RHE@10 mA cm^{-2}	[4]
NiS/Co_3S_4/Ni_3S_2/NF	1.52 V vs. RHE@10 mA cm^{-2}	[5]
Co_9S_8@FeS_2	1.44 V vs. RHE@10 mA cm^{-2}	[6]
Ni_3S_2/$NiMoO_4$	1.5 V vs. RHE@10 mA cm^{-2}	[7]
$MoNi_4$	1.462 V vs. RHE@10 mA cm^{-2}	[8]
Ni/NiMoN	1.42 V vs. RHE@10 mA cm^{-2}	[9]
CoNi-LDH/Fe-MOF/NF	1.55 V vs. RHE@100 mA cm^{-2}	[10]
Mo-Co_9Se_8/Fe-NiSe/$NiSe_2$/NF	1.529 V vs. RHE@10 mA cm^{-2}	[11]
$NiCoS_x$/Nf	1.41 V vs. RHE@10 mA cm^{-2} 1.55 V vs. RHE@100 mA cm^{-2}	[12]
Ni_3S_2@Ni_3Se_2/Nf	1.45 V vs. RHE@10 mA cm^{-2}	[13]
CeO_2/$Co(OH)_2$/FeS@NF	1.41 V vs. RHE@10 mA cm^{-2}	[14]
NiFeS@NiMoP/NF	1.40 V vs. RHE@10 mA cm^{-2}	[15]
This work	1.381 V vs. RHE@10 mA cm^{-2} 1.440 V vs. RHE@50 mA cm^{-2} 1.51 V vs. RHE@100 mA cm^{-2}	/

References:

[1] Yin, R.; Wang, Z.; Zhang, J.; Liu, W.; He, J.; Hu, G.; Liu, X., Tunable NiSe-Ni_3Se_2 Heterojunction for Energy-Efficient Hydrogen Production by Coupling Urea

Degradation. *Small Methods.* **2025**, 2401976.

[2] Duan, Y.; Sultana, F.; Zhang, X.; Yan, X.; Du, X.; Shi, M.; Zhang, P.; Qin, X.; Qian, K.; Li, T.; Tan, M.; Li, R., Optimizing Nickel-Based catalysts for UOR: The role of W interface in nickel-selective oxidation reaction (NSOR) enhancement. *Chem. Eng. J.* **2025,** *512*, 162215.

[3] Li, H.; Pu, Y.; Li, W.; Yan, Z.; Deng, R.; Shi, F.; Zhao, C.; Zhang, Y.; Duan, T., Sulfur-Vacancy Engineering Accelerates Rapid Surface Reconstruction in Ni-Co Bimetal Sulfide Nanosheet for Urea Oxidation Electrocatalysis. *Small* **2024,** *20* (42), 2403311.

[4] Guo, J.; Zhang, H.; Yang, Y.; Wei, M.; Zhang, H., V-Doping coupled H_2O_2 pre-oxidation synergistically promote NiCo-LDH for urea oxidation-assisted hydrogen production. *J. Mater. Chem. A.* **2024,** *12* (27), 16780-16792.

[5] Dou, M.; Wang, W.; Liu, X.; Yao, M.; Ding, K.; Lin, W.; Cao, X.; Li, C.; Li, S.; Chen,Y., Heterostructured NiS/Co_3S_4/Ni_3S_2 Nanomaterials for Urea Oxidation-Assisted Hydrogen Production. *ACS Appl. Nano Mater.* **2024,** *7* (20), 23604-23616.

[6] Liu, W.; Teng, Z.; An, B.; Dong, J.; Li, N.; Gao, Y.; Ge, L., Asymmetric electronic structure effects in Co_9S_8@FeS_2 core-shell nanostructures for highly efficient overall water splitting by modulating d-p orbital hybridization. *Chem. Eng. J.* **2025,** *504*, 158932.

[7] Chen, F.; Ji, S.; Liu, Q.; Wang, H.; Liu, H.; Brett, D. J. L.; Wang, G.; Wang, R., Rational Design of Hierarchically Core–Shell Structured Ni_3S_2@$NiMoO_4$ Nanowires for Electrochemical Energy Storage. *Small* **2018,** *14* (27), 1800791.

[8] Wang, X.; Sha, N.; Zhao, N.; Su, T.; Lv, C.; Yang, L.; Xie, Y.; Ye, K., Structure engineering and surface reconstruction enabling $MoNi_4$ hollow nanocube for efficient urea-assisted water electrolysis. *Chem. Eng. J.* **2024,** *499*, 156119.

[9] Fan, Y.; Gu, Y.; Wang, D.; Jiao, Y.; Wu, A.; Tian, C., Hollow NiMo-based nitride heterojunction with super-hydrophilic/aerophobic surface for efficient urea-assisted hydrogen production. *J. Energy Chem.* **2024,** *95*, 428-439.

[10] Bian, Q.-N.; Guo, B.-S.; Tan, D.-X.; Zhang, D.; Kong, W.-Q.; Wang, C.-B.; Feng,

Y.-Y., Constructing CoNi-LDH/Fe MOF/NF Heterostructure Catalyst for Energy-Efficient OER and UOR at High Current Density. *ACS Appl. Mater. Interfaces.* **2024,** *16* (12), 14742-14749.

[11] Wang, H.; Du, X.; Zhang, X., Transition metal-based selenide materials derived from ZIF-67 as efficient urea and seawater splitting electrocatalyst. *Renew. Energy.* **2025,** *244*, 122663.

[12] Li, G.-L.; Deng, F.; Ma, T.-G.; Shi, Y.-H.; Liao, Z.-Q.; Liu, J.-J.; Yan, Y.; Wang, E., Synergistically engineering of amorphous-crystalline heterostructure and lattice defects on hierarchical $NiCoS_x$/NF for efficient overall urea-assisted water splitting. *Int. J. Hydrog. Energy.* **2024,** *92*, 324-332.

[13] Ai, T.; Bai, M.; Bao, W.; Han, J.; Wei, X.; Zou, X.; Hou, J.; Zhang, L.; Deng, Z.; Zhang, Y., Engineering high-valence nickel sites in Ni_3S_2/Ni_3Se_2 architectures enabling urea-assisted hydrogen evolution reactions. *Green Chem.* **2024,** *26* (24), 11934-11947.

[14] Duan, F.; Hu, Y.; Lin, J.; Li, M.; Wu, H.; Cui, Z.; Fang, C., Construction of CeO_2/$Co(OH)_2$/FeS@NF nanosheet arrays for high-performance electrocatalytic oxygen evolution/urea oxidation, and overall water/urea splitting reactions. *Int. J. Hydrog. Energy.* **2024,** *94*, 706-715.

[15] Yang, S.; Wen, T.; Gong, Y., Optimized crystalline/amorphous NiFeS@NiMoP on nickel foam as dual-functional electrocatalysts for urea-water splitting. *Int. J. Hydrog. Energy.* **2024,** *68*, 834-842.